Mechanics of Materials 175 (2022) 104504

Contents lists available at ScienceDirect

Mechanics of Materials

journal homepage: www.elsevier.com/locate/mechmat

Buckling behavior and damage mechanism analysis of fiber-reinforced shape memory polymer composites

Zhengxian Liu [a], Xin Lan [a,**], Liwu Liu [b], Wenfeng Bian [c], Yanju Liu [b], Jinsong Leng [a,*]

[a] Centre for Composite Materials and Structures, Harbin Institute of Technology (HIT), Harbin, 150001, People's Republic of China
[b] Department of Astronautical Science and Mechanics, Harbin Institute of Technology (HIT), Harbin, 150080, People's Republic of China
[c] Department of Civil Engineering, Harbin Institute of Technology (HIT), Weihai, 264209, People's Republic of China

ARTICLE INFO

Keywords:
Shape memory polymer composites
Buckling behavior
Damage mechanism
Theoretical analysis

ABSTRACT

Shape memory polymer composites (SMPCs) are emerging as an attractive material for space deployable structures due to their variable stiffness, programmable deformation, high packing ratio, and controllable deployment. However, the research on the deformation behaviors and damage mechanisms of SMPC was scarce. The buckling behaviors and damage mechanisms of out-of-plane buckling and in-plane buckling of fiber-reinforced SMPC were investigated in this study. The expression and evolution law of strain energy and key parameters of fiber buckling were studied. The effects of material parameters and size parameters on damage mode and critical damage curvature were analyzed quantitatively. It was found that in-plane buckling was more likely to occur without external constraints. The damage modes of in-plane buckling are classified as delamination, matrix cracking and fiber tensile fracture. Out-of-plane buckling is more susceptible to damage and has one more fiber buckling fracture damage mode than in-plane buckling. When the fiber volume content is below a certain value, only fiber tensile fracture damage mode will appear, regardless of the thickness. Delamination is more likely to occur in cases of out-of-plane buckling, and matrix cracking is more frequent in cases of in-plane buckling. Subsequently, the correctness of the theoretical analysis was verified by the bending test. The theoretical analysis in this study provides a theoretical foundation for SMPCs-based structural design.

1. Introduction

As one of the research hotspots in the field of smart materials, shape memory polymers (SMPs) can conduct shape programming under external stimulation. After removing the stimulation, they can keep the temporary shape (Boudjellal et al., 2020; Luo et al., 2021; Melly et al., 2021; Patel and Purohit, 2018; Shojaei et al., 2015; Xie, 2011). Once they are activated again, they can recover to their permanent shape. Otherwise, they will remain stable. SMPs can be triggered by thermal, light, electrical, magnetic and solution (Glock et al., 2015; Gu et al., 2019; Leng et al., 2009; Lu et al., 2015; Wang et al., 2015). The development and application of SMPs are currently advancing rapidly, with applications in aerospace engineering, biomedicine, flexible electronics and soft robots (Liu et al., 2018; Luo et al., 2022; Shin et al., 2019; Xia et al., 2021; Zhang et al., 2019).

Shape memory polymers have the characteristics of variable stiffness, programmable shape, large deformation and facile preparation. However, they are difficult to be directly used as structural materials because of their low stiffness, strength and recovery force (Garces and Ayranci, 2021; Melly et al., 2020; Xin et al., 2019). To make up for inherent shortcomings and expand application range, reinforcements are added inside SMPs, such as particles (Das et al., 2009; Shaffer and Windle, 1999; Thostenson and Chou, 2002; Yoonessi et al., 2012), nanofibers (Dong et al., 2014; Dong and Ni, 2015), short fibers (Leng et al., 2007, 2008) and long fibers (Gall et al., 2000; Li et al., 2020; Wei et al., 1998). Fiber-reinforced shape memory polymer composites (SMPCs) are often employed in space deployable structures due to their excellent mechanical properties (Liu et al., 2014). SMPCs as a driving structure need to be bent or crimped to obtain a high storage ratio. For thermo-responsive fiber-reinforced SMPCs, when the external temperature gradually increases to the glass transition temperature (Tg), the matrix modulus gradually decreases. At this time, when the shear modulus in the compressing region is not enough to resist the transverse deformation of the fibers during bending, the fibers will buckle, which is

* Corresponding author.
** Corresponding author.
E-mail addresses: lanxin@hit.edu.cn (X. Lan), lengjs@hit.edu.cn (J. Leng).

https://doi.org/10.1016/j.mechmat.2022.104504
Received 2 July 2022; Received in revised form 29 September 2022; Accepted 15 October 2022
Available online 22 October 2022

also the large deformation mechanism of unidirectional fiber-reinforced SMPCs (Lan et al., 2014).

Currently, there have been some studies on the buckling mechanism and theory of unidirectional fiber-reinforced SMPCs (Guo et al., 2017; Zhang et al., 2018). Based on summarizing the previous micro-buckling solutions of SMPCs, Francis et al. (2007) proposed a new set of micro-buckling analytical solutions. In this work, the expressions of the neutral surface position and half-wavelength were solved from the perspective of strain energy. This model provides a great basis for the prediction of SMPC. Lan et al. (2014) considered the compressing and non-buckling region and developed a strain energy expression of the SMPC thermodynamic system. At the same time, the damage morphology was observed. In addition, Gall et al. (2016) observed the morphology of fabric-reinforced SMPC after bending through a scanning electron microscope. It was found that the fiber occurred out-of-plane buckling, resulting in matrix cracking, while the diffuse in-plane buckling was elastic and non-destructive. However, there are still some gaps in the current research, such as there is no detailed comparison between in-plane buckling and out-of-plane buckling for SMPC; the damage mechanism and damage limit were not analyzed theoretically. Hence, it is difficult to meet the needs of structural design.

The micromechanical analysis of out-of-plane and in-plane buckling of unidirectional fiber-reinforced SMPC was carried out in this study. The strain energy of in-plane and out-of-plane buckling systems was calculated. Simultaneously, the key parameters of the two systems were derived and compared by using the minimum energy principle. The stress state of the matrix and fiber of in-plane and out-of-plane buckling were analyzed, and the damage modes and critical damage curvature were obtained. Finally, the bending test was performed to verify the correctness of the theoretical analysis.

2. Out-of-plane buckling analysis

According to the buckling direction of the fiber, there are two buckling modes: out-of-plane buckling and in-plane buckling (Xiong et al., 2014). The out-of-plane buckling refers to fiber buckling in the thickness direction, while in-plane buckling refers to fiber buckling in the width direction. It was found that the buckling direction of fiber is mainly related to external constraints. The out-of-plane buckling is prone to occur when the constraint fiber displacement is in the width direction, while the in-plane buckling is more likely to occur when the constraint fiber displacement is in the thickness direction.

2.1. Strain energy of out-of-plane buckling

This study found that when unidirectional fiber reinforced SMPC is bent at Tg and the displacement in the width direction is restrained, the fiber is more prone to out-of-plane buckling. To study the micro-mechanisms of unidirectional fiber-reinforced SMPC, the strain energy of the out-of-plane buckling system was deduced. Fig. 1(a) and (b) show the out-of-plane buckling morphology during bending. The shape of fiber buckling presents the sine/cosine wave according to the minimum energy principle, hence the shape function of the fiber buckling can be represented as (Lan et al., 2014):

$$w = A\cos\left(\frac{\pi x}{\lambda}\right) \tag{1}$$

where λ and A are the half-wavelength and amplitude of the fiber buckling, respectively. The amplitude of the fiber buckling can be expressed as (Lan et al., 2014):

$$A = \frac{2\lambda}{\pi}\sqrt{\kappa(z - z_{ns})} \tag{2}$$

where κ is the bending curvature. By introducing Eq. (2) into Eq. (1), the shape function of fiber buckling can be given as follows:

$$w = \frac{2\lambda}{\pi}\sqrt{\kappa(z - z_{ns})}\cos\left(\frac{\pi x}{\lambda}\right) \tag{3}$$

The deformation model diagram of buckling region is shown in Fig. 1 (c). The matrix has a mixed deformation of the shear, compression and

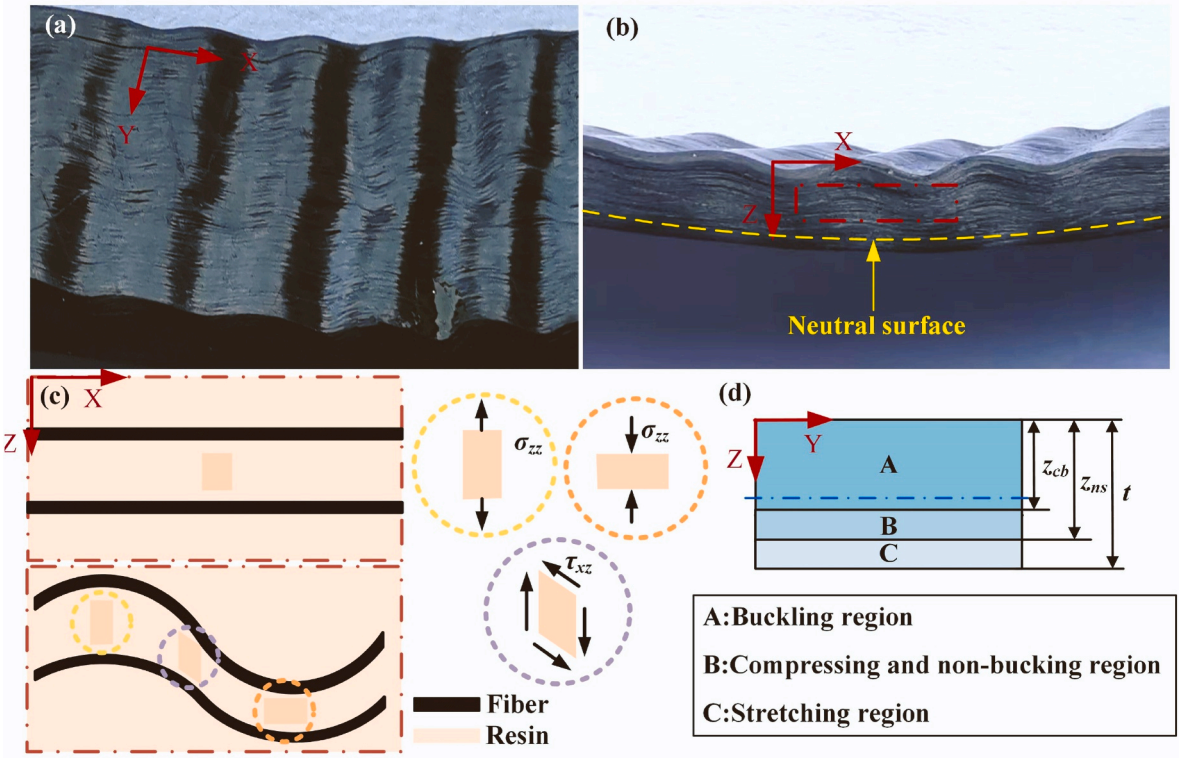

Fig. 1. Out-of-plane buckling diagram of SMPC; (a) X–Y view; (b) X-Z view; (c) Deformation model diagram of buckling region; (d) Cross-section division.

tension in the buckling region. The compressive deformation of the matrix in the X-direction of the buckling region is very small. Therefore, the compressive deformation in the buckled matrix is ignored in this study (Francis et al., 2007; Xiong et al., 2008). The buckling deformation of the fiber leads to the shear deformation of the matrix, whereas the compression and tension deformation occurs owing to the different buckling amplitudes of the adjacent fibers in the X-Z plane. According to the stress state of the fiber, the cross-section can be divided into three regions, namely buckling region, compressing and non-buckling region, and stretching region (as shown in Fig. 1(d)). Z_{ns} and z_{cb} denote the neutral surface position and the critical buckling position respectively, and t is the thickness of SMPC. The material parameters and dimensional parameters used in this study are shown in Table 1 and Table 2.

The epoxy-based SMP studied in this study is in the rubbery state at Tg, and the material is linear elastic (Liu et al., 2020). The matrix and fiber were regarded as linear elastic materials in this study, and the total strain energy of the system is:

$$U_T = \frac{1}{2}\int \varepsilon_{ij}\sigma_{ij}dv = \frac{1}{2}\int \left(\varepsilon_{xx}\sigma_{xx} + \varepsilon_{yy}\sigma_{yy} + \varepsilon_{zz}\sigma_{zz} + \tau_{xy}\gamma_{xy} + \tau_{yz}\gamma_{yz} + \tau_{xz}\gamma_{xz}\right)dv \tag{4}$$

Through the deformation analysis of the matrix and fiber in the out-of-plane buckling system, the matrix is mainly subjected to the compressive and tensile deformations in the Z-direction, and the shear deformation in the X-Z plane in the buckling region, and compressive and tensile deformations in the non-buckling region. The fiber is mainly subjected to buckling deformation in the buckling region, and compressive and tensile deformations deformation in the non-buckling region. Therefore, the total strain energy of the system can be transformed into:

$$U_T^{out} = U_{xx}^{out} + U_{xz}^{out} + U_{fb}^{out} + U_{zz}^{out} \tag{5}$$

where *Uout T* denotes the total strain energy of the out-of-plane buckling system; *Uout xx* denotes the strain energy of the composite in the non-buckling region; *Uout xz* denote the shear strain of the matrix caused by γ_{xz}; *Uout fb* denotes the strain energy of fiber buckling; *Uout zz* represents the strain energy of the matrix in the Z-direction in the buckling region.

Based on the equal strain assumption of fiber and matrix and the parallel model of composite, the strain energy of composite in the non-buckling region can be expressed as:

$$U_{xx}^{out} = \frac{1}{2}\int_{z_{cb}}^{t}\int_0^b\int_0^l E\varepsilon_{xx}^2 dxdydz \tag{6}$$

where $E=\nu_f E_f+\nu_m E_m$, ν_f and ν_m represent volume content of the fiber and matrix, respectively; b and l represent the width and length of SMPC, respectively. The tensile/compressive strain of fiber and matrix in the non-buckling region can be expressed as:

$$\varepsilon_{xx} = \kappa(z - z_{ns}) \tag{7}$$

Eq. (8) can be obtained by incorporating Eq. (7) into Eq. (6):

$$U_{xx}^{out} = \frac{blE\kappa^2}{6}\left[(t - z_{ns})^3 + (z_{ns} - z_{cb})^3\right] \tag{8}$$

During bending deformation, deformation along the circumferential direction of the curve is restricted by complete restraints (displacement along the circle of $u = 0$, thickness direction displacement $w \neq 0$) (Lan et al., 2014). Therefore, the shear stress of the matrix can be expressed as Eq. (9).

$$\gamma_{xz} = \frac{\partial u}{\partial z} + \frac{\partial w}{\partial x} = \frac{\partial w}{\partial x} = -2\sqrt{\kappa(z - z_{ns})}\sin\left(\frac{\pi x}{\lambda}\right) \tag{9}$$

According to Eq. (3), the amplitude of adjacent fibers in the X-Z plane is different, which will lead to the shear strain of the matrix. The strain energy of the matrix caused by shear strain γ_{xz} can be expressed as Eq. (10). Substitute Eq. (9) into Eq. (10) can obtain Eq. (11):

$$U_{xz}^{out} = \frac{1}{2}\int_0^{z_{cb}}\int_0^b\int_0^l \nu_m G_m \gamma_{xz}^2 dxdydz \tag{10}$$

$$U_{xz}^{out} = \frac{bl\nu_m G_m \kappa}{2}\left[z_{ns}^2 - (z_{ns} - z_{cb})^2\right] \tag{11}$$

where G_m denotes the shear modulus of the matrix. According to Eq. (3). The different amplitudes of the adjacent fibers in the X-Z plane result in compressive/tensile deformation. The compressive/tensile strain ε_{zz} of the matrix in the Z-direction can be expressed as:

$$\varepsilon_{zz} = \frac{\partial w}{\partial z} = -\frac{\kappa\lambda}{\pi\sqrt{\kappa(z_{ns} - z)}}\cos\left(\frac{\pi x}{\lambda}\right) \tag{12}$$

The compressive/tensile strain energy of the matrix in the Z-direction of the buckling region can be expressed as:

$$U_{zz}^{out} = \frac{1}{2}\int_0^{zcb}\int_0^l\int_0^b \nu_m E_m \varepsilon_{zz}^2 dxdydz \tag{13}$$

Eq. (14) can be obtained by bringing Eq. (12) into Eq. (13):

$$U_{zz}^{out} = \frac{bl\nu_m E_m \lambda^2 \kappa}{4\pi^2}\ln\left(\frac{z_{ns}}{z_{ns} - z_{cb}}\right) \tag{14}$$

The buckling shape of the fiber in the single layer is completely consistent, hence the buckling strain energy of the single-layer fiber can be expressed as:

$$U_{f_{(\text{one layer})}}^{out} = \frac{b}{h}U_{f_{(\text{single fibre})}}^{out} \tag{15}$$

Where h is the center distance between adjacent fibers ($h = d\sqrt{\pi\nu_f}/2\nu_f$). When the fiber volume content is 20%, then the h comes to 0.01 mm, which is much less than the thickness of SMPC. The strain energy of fiber buckling can be expressed as:

$$U_{fb}^{out} = \sum_{n=1}^{m}\frac{b}{h^2}U_{f_{(\text{one layer})}}^{out} \tag{16}$$

where $n = 1, 2, 3\ m$, $m = z_{cb}/h$, and m is a positive integer. Since z_{ns} is much larger than h, the fiber buckling strain energy of the out-of-plane buckling system can be simply expressed as:

$$U_{fb}^{out} = \frac{2bl\pi^2\nu_f E_f I_f \kappa}{d^2\lambda^2}\left[(z_{ns} - z_{fa})^2 - (z_{ns} - z_{cb})^2\right] \tag{17}$$

Considering the bending problem of small strain and large displacement of the buckling beam in the study, it is reasonable to use the buckling equation expression to calculate the strain energy of the fiber in the buckling region (Francis et al., 2007; Lan et al., 2014).

Table 1
Material parameters of the matrix and carbon fiber.

Material	Tensile modulus (MPa)	Shear modulus (MPa)	Poisson's ratio	Shear strength (MPa)	Tensile strength (MPa)
Matrix (T_g)	32	11	0.45	7.8	8.2
Fiber	45000	–	0.3	–	1100

Table 2
Dimension parameters of SMPC.

Material	Thickness (mm)	Width (mm)	Length (mm)	Fiber volume content (%)	Fiber diameter (mm)
SMPC	2	5	30	20	0.008

Substituting the partial energy expression into the total strain energy expression of the out-of-plane buckling system, the following can be obtained:

$$U_T^{out}=\frac{blE\kappa^2}{6}\left[(t-z_{ns})^3+(z_{ns}-z_{cb})^3\right]+\frac{bl\nu_m G_m\kappa}{2}z_{cb}(2z_{ns}-z_{cb})+\frac{bl\nu_m E_m\lambda^2\kappa}{4\pi^2}\ln\left(\frac{z_{ns}}{z_{ns}-z_{cb}}\right)+\frac{2bl\pi\nu_f E_f I_f\kappa}{d^2\lambda^2}z_{cb}(2z_{ns}-z_{cb}) \tag{18}$$

2.2. Key parameters analysis

The compressing and non-buckling region is very small compared with the stretching region and the buckling region (Lan et al., 2014). When the compressing and non-buckling region is neglected, the strain energy expression can be presented in Eq. (19).

$$U_T^{out}=\frac{blE\kappa^2}{6}(t-z_{ns})^3+\frac{bl\nu_m G_m\kappa}{2}z_{ns}^2+\frac{bl\nu_m E_m\lambda^2\kappa}{4\pi^2}\ln\left[\frac{4z_{ns}\sqrt{v_f}}{d\sqrt{\pi}}\right]+\frac{2bl\pi\nu_f E_f I_f\kappa}{\lambda^2 d^2}z_{ns}^2 \tag{19}$$

Fig. 2(a) shows the strain energy variation of the out-of-plane buckling system with the relative neutral surface position. It is assumed that the curvature and the half-wavelength of fiber buckling are constant, and the neutral surface position (z_{ns}) changes from $t/2$ to t. It was observed that *Uout xx* and *Uout xz* are much larger than other strain energies. Therefore, *Uout fb* and *Uout zz* can be ignored when solving the neutral surface position, and the total strain energy expression can be changed to Eq. (20) (Francis et al., 2007; Lan et al., 2019). At the same time, there exists a minimum energy for the out-of-plane buckling system with the change of the relative neutral surface position. Therefore, the partial derivatives of z_{ns} and z_{cb} can be obtained by utilizing the minimum energy principle.

$$\widehat{U}(z_{cb},z_{ns})=U_{xx}^{out}+U_{xz}^{out} \tag{20}$$

$$\begin{cases}\dfrac{\partial\widehat{U}(z_{cb},z_{ns})}{\partial z_{cb}}=0\\ \dfrac{\partial\widehat{U}(z_{cb},z_{ns})}{\partial z_{ns}}=0\end{cases} \tag{21}$$

By solving Eq. (21), the positions of the neutral surface and critical buckling can be obtained:

$$\begin{cases}z_{ns}=t-\dfrac{C}{\kappa}\left(\sqrt{1+\dfrac{2\kappa t}{C}}-1\right)\\ z_{cb}=t-\dfrac{C}{\kappa}\left(\sqrt{1+\dfrac{2\kappa t}{C}}+1\right)\end{cases} \tag{22}$$

where $C=\nu_m G_m/(\nu_m E_m+\nu_f E_f)$. The half-wavelength is only related to strain energy *Uout zz* and *Uout fb*. Fig. 2(b) shows the variations of strain energy *Uout zz* and *Uout fb* with half-wavelength. The half-wavelength expression of the out-of-plane buckling system can be solved by using the minimum energy principle (as shown in Eq. (23)).

$$\lambda^{out}=\left[\frac{8\pi^3\nu_f E_f I_f\left(z_{ns}^2-\frac{4C^2}{\kappa^2}\right)}{d^2\nu_m E_m\ln\left(\frac{z_{ns}\kappa}{2C}\right)}\right]^{\frac{1}{4}} \tag{23}$$

where I_f is the cross-sectional moment of inertia of the fiber. The amplitude expression can be obtained according to the relationship between half-wavelength and amplitude:

$$A^{out}=\frac{2\sqrt{\kappa(z_{ns}-z)}}{\pi}\left[\frac{8\pi^3\nu_f E_f I_f\left(z_{ns}^2-\frac{4C^2}{\kappa^2}\right)}{d^2\nu_m E_m\ln\left(\frac{z_{ns}\kappa}{2C}\right)}\right]^{\frac{1}{4}} \tag{24}$$

The expression of bending moment and equivalent bending stiffness can be deduced as follows:

$$M=\frac{\partial U_T}{l\partial\kappa} \tag{25}$$

$$EI_e=\frac{M}{\kappa} \tag{26}$$

2.3. Stress analysis

To study the damage mode of SMPC during bending, the deformation analysis of the matrix and fiber of the out-of-plane buckling system was carried out. The matrix stress can be divided into compressive and tensile stress in the X-direction, compressive and tensile stress in the Z-direction and shear stress in the X-Z plane.

The main deformation modes of fibers during bending can be divided into buckling, compression and tension, in which the curvature of fiber buckling in the buckling region can be stated as:

$$\kappa_{fb}=\frac{|y''|}{(1+y'^2)^{\frac{3}{2}}}=\frac{\left|\frac{A\pi^2}{\lambda^2}\cos\left(\frac{\pi x}{\lambda}\right)\right|}{\left[1+\frac{A^2\pi^2}{\lambda^2}\sin^2\left(\frac{\pi x}{\lambda}\right)\right]^{\frac{3}{2}}} \tag{27}$$

The amplitude of fiber buckling is the largest at $z=0$. When $x=n\lambda$, the fiber buckling curvature reaches the maximum, so the maximum stress of fiber buckling can be expressed as:

$$\sigma_{fb,\max}^{out}=E_f\varepsilon_{fb,\max}=\frac{E_f dA\pi^2}{2\lambda^2} \tag{28}$$

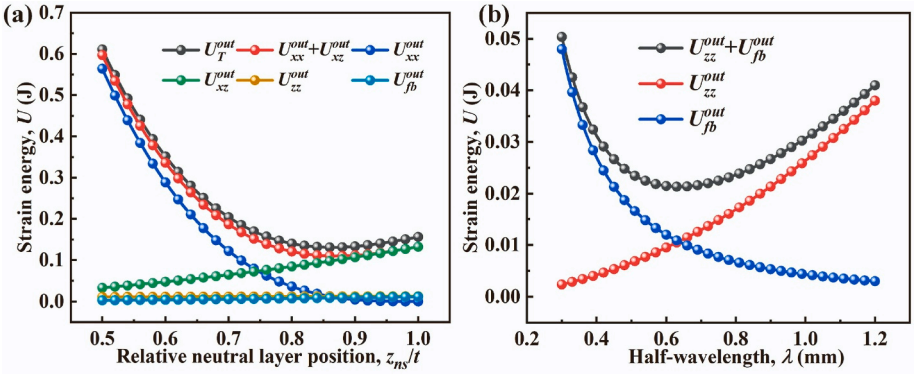

Fig. 2. (a) Partial strain energy variation with relative neutral surface position ($\lambda=0.68$ mm, $\kappa=0.05$ mm^{-1}); (b) Strain energy variation of *Uout zz* and *Uout fb* with half-wavelength ($\kappa=0.05$ mm^{-1}, $z_{ns}=1.8$ mm).

where E_f and d represent the modulus and diameter of the fiber, respectively. In the non-buckling region, the fiber is subjected to compressive/tensile deformation, and the compressive/tensile stress of the fiber is as follows:

$$\sigma_{fxx}^{out} = E_f \varepsilon_{xx} = E_f \kappa (z - z_{ns}) \tag{29}$$

Due to the existence of the buckling region, the tensile stress of the fiber in the non-buckling region is greater than the compressive stress of the fiber. When $z = t$, the tensile stress of the fiber reaches the maximum:

$$\sigma_{fxx,\max}^{out} = E_f \kappa (t - z_{ns}) \tag{30}$$

The compressive/tensile stress of the matrix in the Z-direction in the buckling region can be expressed as follow:

$$\sigma_{zz} = E_m \varepsilon_{zz} = \frac{E_m \kappa \lambda}{\pi \sqrt{\kappa (z_{ns} - z)}} \cos\left(\frac{\pi x}{\lambda}\right) \tag{31}$$

When $z = z_{cb}$, $x = n\gamma$ ($n = 0,1,2\cdots\cdots$), the compressive/tensile stress of the matrix reaches the maximum:

$$\sigma_{zz,\max} = \frac{E_m \kappa \lambda}{\pi \sqrt{\kappa (z_{ns} - z_{cb})}} \tag{32}$$

The shear stress of the matrix in the X-Z plane in the buckling region can be stated as:

$$\tau_{xz} = G_m \gamma_{xz} = -2G_m \sqrt{\kappa (z_{ns} - z)} \sin\left(\frac{\pi x}{\lambda}\right) \tag{33}$$

When $z = 0$, $x = n\gamma/2$ ($n = 0,1,2\cdots\cdots$), the shear stress reaches the maximum value:

$$\tau_{xz,\max} = 2G_m \sqrt{\kappa z_{ns}} \tag{34}$$

The stress analysis indicates that the maximum stress of the matrix in the buckling region appears at $z = 0$ or $z = z_{cb}$. The shear stress of the matrix at $z = 0$ can be written as Eq. (35). The evolution law of shear stress $\tau out\ z{=}0$ with X-direction position and bending curvature is shown in Fig. 3(a). The results reveal that when $x = n\gamma/2$ ($n = 0,1,2\cdots\cdots$), shear stress $\tau out\ z{=}0$ approaches the maximum (as shown in Eq. (36)).

$$\tau_{z=0}^{out} = \sqrt{\frac{1}{4}\left(\frac{E_m \kappa \lambda}{\pi \sqrt{\kappa z_{ns}}} \cos\left(\frac{\pi x}{\lambda}\right)\right)^2 + 4G_m^2 \kappa z_{ns} \sin^2\left(\frac{\pi x}{\lambda}\right)} \tag{35}$$

$$\tau_{z=0}^{out}, \max = 2G_m \sqrt{\kappa z_{ns}} \tag{36}$$

According to the stress analysis of the matrix at $z = z_{cb}$, the shear stress of the matrix can be given as Eq. (37). The evolution law of shear stress $\tau out\ z{=}zcb$ with X-direction position and bending curvature is shown in Fig. 4(b). The results indicate that $x = n\gamma$ ($n = 0,1,2\cdots\cdots$), shear stress $\tau out\ z{=}zcb$ approaches the maximum (as shown in Eq. (38)).

$$\tau_{z=z_{cb}}^{out} = \sqrt{\frac{1}{4}\left(\frac{E_m \kappa \lambda}{\pi \sqrt{\kappa (z_{ns} - z_{cb})}} \cos\left(\frac{\pi x}{\lambda}\right)\right)^2 + 4G_m^2 \kappa (z_{ns} - z_{cb}) \sin^2\left(\frac{\pi x}{\lambda}\right)} \tag{37}$$

$$\tau_{z=z_{cb}}^{out}, \max = \frac{E_m \kappa \lambda}{2\pi \sqrt{2C}} \tag{38}$$

To study the damage sequence and evolution law caused by shear stress at $z = 0$ and $z = z_{cb}$, the shear stress ratio at $z = 0$ and $z = z_{cb}$ can be obtained by comparing Eq. (36) with Eq. (38):

$$\frac{\tau_{z=0}^{out}, \max}{\tau_{z=z_{cb},\max}^{out}} = \frac{2\pi G_m \sqrt{2C\kappa z_{ns}}}{\kappa E_m \lambda} \tag{39}$$

2.4. Critical damage curvature

To study the damage limit of out-of-plane buckling of unidirectional fiber-reinforced SMPC, the critical damage of composite was judged according to the internal stress analysis and strength theory. The analysis reveals that the matrix stress at the dangerous point is mainly shear stress, so the maximum shear stress criterion is used to assess the matrix cracking damage at $z = 0$ and the delamination damage at $z = z_{cb}$. The fiber stress at the dangerous point is mainly tensile, so the maximum tensile stress criterion is used to judge whether the fiber will break. The buckling surface ($z = 0$) and the critical buckling position ($z = z_{cb}$) are dangerous points of the matrix, while the maximum buckling curvature position ($z = 0$) and the tensile surface ($z = t$) are the dangerous points of the fiber. The shear stress of the matrix at $z = 0$ reaches the shear strength, which represents the matrix cracking damage; the shear stress of the matrix at $z = z_{cb}$ reaches the shear strength, which signifies the delamination damage at the critical buckling position; the tensile stress of the fiber at $z = t$ reaches the tensile strength, which indicates the fiber tensile fracture damage; the tensile stress of the fiber at $z = 0$ reaches the shear strength, which represents the fiber buckling fracture damage. The stress of the matrix and fiber must be smaller than their respective strengths during bending. As a result, the stress of matrix and fiber at the dangerous point in SMPC should match the following conditions:

$$\tau_{z=0}^{out}, \max \le \tau_s,\ \tau_{z=z_{cb}}^{out}, \max \le \tau_s,\ \sigma_{fxx}^{out}, \max \le \sigma_{sf},\ \sigma_{fb}^{out},\ \max \le \sigma_{sf} \tag{40}$$

where τ_s and σ_{sf} represent the shear strength of the matrix and the tensile strength of the fiber, respectively.

In this study, the bending curvature corresponding to the critical damage was taken as the damage limit of SMPC. Substituting Eqs. ((28), (30), (36) and (38) into Eq. (40), the critical damage curvature can be obtained. The critical damage curvature of unidirectional fiber-

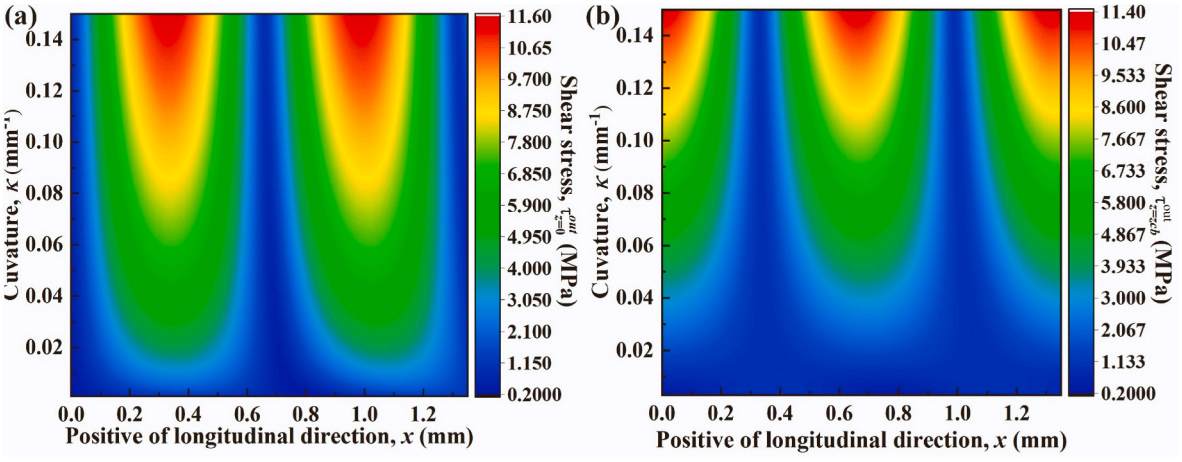

Fig. 3. Shear stress distribution along the X direction during bending in the out-of-plane buckling: (a) shear stress $\tau out\ z{=}0$ (b) shear stress $\tau out\ z{=}zcb$.

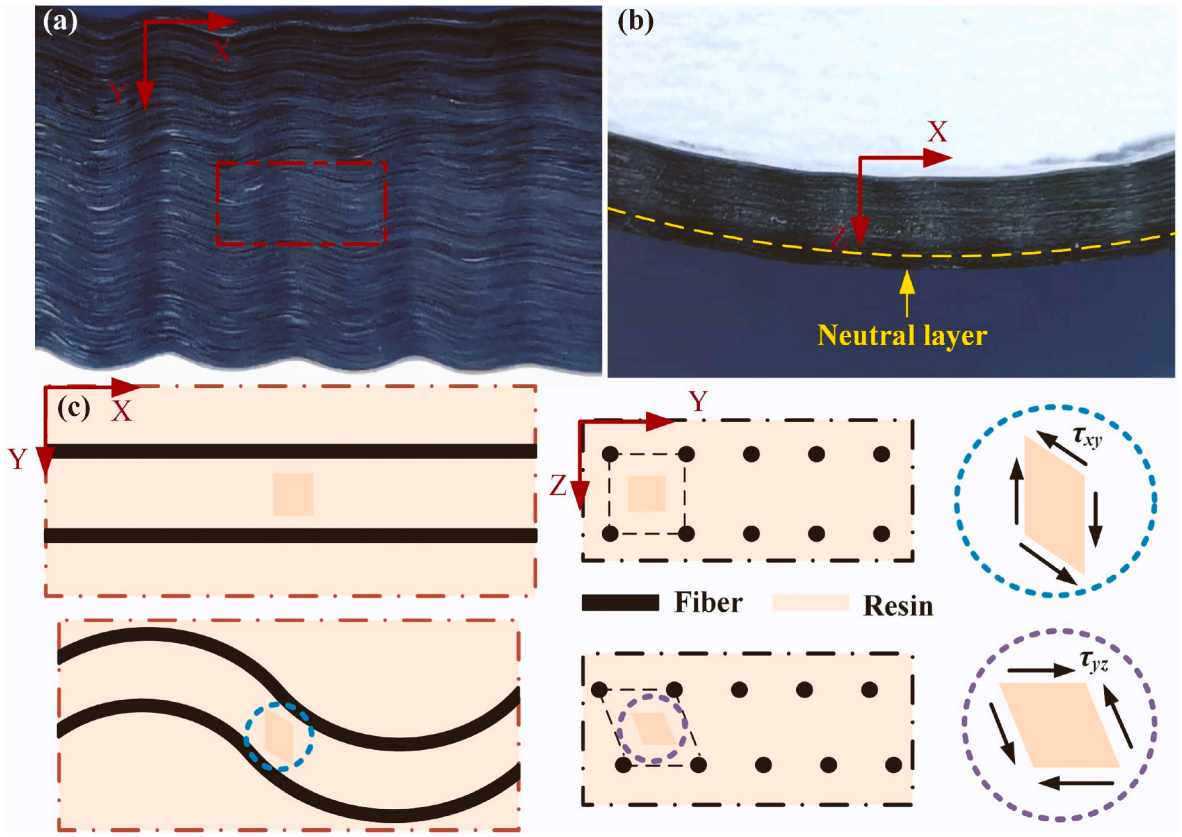

Fig. 4. Out-of-plane buckling diagram of SMPC; (a) X–Y view; (b) X-Z view; (c) Deformation model diagram of buckling region.

reinforced SMPC during bending was the minimal value of the bending curvature corresponding to the above stresses:

$$\kappa_{cf}^{out} = \min\left\{\kappa_{cf,z=0}^{out}, \kappa_{cf,z=z_{cb}}^{out}, \kappa_{cf,fxx}^{out}, \kappa_{cf,fb}^{out}\right\} \tag{41}$$

where κout cf represents the critical damage curvature; κout cf,z=*0* and κout cf,z=*zcb* represent matrix cracking and delamination damage at $z = 0$ and $z = z_{cb}$ respectively; κout cf,*fxx* and κout cf,*fb* represent the critical damage curvature of fiber tensile fracture and buckling fracture at $z = t$ and $z = 0$, respectively.

3. In-plane buckling analysis

3.1. Strain energy of in-plane buckling

When unidirectional fiber-reinforced SMPC bend around a cylinder at Tg, the fibers can only buckle in plane due to the constraint of thickness direction displacement. The surface morphology of the in-plane buckling is shown in Fig. 4(a) and (b). It can be observed that the buckling morphology of fibers is wavy, and the adjacent fibers show the same change law. In accordance with the out-of-plane buckling, the cross-section can be divided into buckling region, compressing and non-buckling region and tensile region (as shown in Fig. 1(d)).

Fig. 4(c) is the deformation model diagram in the X–Y plane and X-Z plane. Similar to the out-of-plane buckling, the geometry of fiber buckling presents a sin/cosine wave, and the shape function of the fiber of the in-plane buckling is given in Eq. (42).

$$y = \frac{2\lambda}{\pi}\sqrt{\kappa(z_{ns} - z)}\cos\left(\frac{\pi x}{\lambda}\right) \tag{42}$$

The fiber buckling direction is solely in the X–Y plane when in-plane buckling occurs (as shown in Fig. 4(c)). The shape function of the fiber in the X–Y plane is uniform. Through the stress analysis of the matrix between fibers, the main deformation modes of the matrix in the X–Y plane are the shear and compressive deformations. Based on the equal strain assumption and the shape function of the fiber, the shear stress of the matrix in the X–Y plane can be expressed as:

$$\gamma_{xy} = \frac{\partial v}{\partial x} + \frac{\partial u}{\partial y} = \frac{\delta y}{\delta x} = -\sqrt{\kappa(z_{ns} - z)}\sin\left(\frac{\pi x}{\lambda}\right) \tag{43}$$

where γ_{xy} represents the shear strain of the matrix in the X–Y plane. According to the shape function expression of the fiber, the amplitude of the fiber in the Z-direction is different. Therefore, the matrix between two adjacent fibers in the Y-Z plane has shear deformation, and the shear strain γ_{yz} of the matrix in the Y-Z plane can be expressed as:

$$\gamma_{yz} = \frac{\partial v}{\partial z} + \frac{\partial w}{\partial y} = \frac{\delta y}{\delta z} = \frac{\kappa\lambda}{\pi\sqrt{\kappa(z_{ns} - z)}}\cos\left(\frac{\pi x}{\lambda}\right) \tag{44}$$

where γ_{yz} represents the shear strain of the matrix in the Y-Z plane. According to the deformation analysis of in-plane buckling, the total strain energy of the in-plane buckling system can be stated as follows:

$$U_T^{in} = U_{xx}^{in} + U_{xy}^{in} + U_{yz}^{in} + U_{fb}^{in} \tag{45}$$

where *Uin T* is the total strain energy of the in-plane buckling system, *Uin xx* is the strain energy of the non-buckling region, *Uin xy* and *Uin yz* are the shear strain energy of the matrix caused by γ_{xy} and γ_{yz}, respectively, and *Uin fb* is the strain energy of fiber buckling. The strain energy of the non-buckling region can be given as follows:

$$\begin{aligned} U_{xx}^{in} &= \frac{1}{2}\int_{z_{cb}}^{t}\int_{0}^{b}\int_{0}^{l} E\varepsilon_{xx}^{2}\,dxdydz \\ &= \frac{blE\kappa^2}{6}\left[(t - z_{ns})^3 + (z_{ns} - z_{cb})^3\right] \end{aligned} \tag{46}$$

The strain energy caused by shear strain γ_{xy} can be expressed as:

$$U_{xy}^{in}=\frac{1}{2}\int_0^{z_{cb}}\int_0^b\int_0^l \nu_m G_m \gamma_{xy}^2 dxdydz = \frac{bl\nu_m G_m\kappa}{2}\left[z_{ns}^2-(z_{ns}-z_{cb})^2\right] \tag{47}$$

The strain energy caused by shear strain γ_{xz} can be represented as:

$$U_{yz}^{in}=\frac{1}{2}\int_0^{z_{cb}}\int_0^l\int_0^b \nu_m G_m \gamma_{yz}^2 dxdydz = \frac{bl\nu_m G_m\lambda^2\kappa}{4\pi^2}\ln\left(\frac{z_{ns}}{z_{ns}-z_{cb}}\right) \tag{48}$$

Since the out-of-plane buckling and in-plane buckling of SMPC during bending are only different in the buckling direction, their shape function of fiber buckling is the same. Similar to the derivation of out-of-plane buckling, the strain energy of fiber buckling is:

$$U_{fb}^{in}=\frac{2bl\pi^2 E_f I_f\kappa}{d^2\lambda^2}\left[z_{ns}^2-(z_{ns}-z_{cb})^2\right] \tag{49}$$

Substituting Eqs. 46–49 into Eq. (45), we yield the total strain energy of the in-plane buckling system:

$$U_T^{in}=\frac{bl E\kappa^2}{6}\left[(t-z_{ns})^3+(z_{ns}-z_{cb})^3\right]+\frac{bl\nu_m G_m\kappa}{2}z_{cb}(2z_{ns}-z_{cb}) +\frac{bl\nu_m G_m\lambda^2\kappa}{4\pi^2}\ln\left(\frac{z_{ns}}{z_{ns}-z_{cb}}\right)+\frac{2\pi bl\nu_f E_f I_f\kappa}{\lambda^2 d^2}z_{cb}(2z_{ns}-z_{cb}) \tag{50}$$

3.2. Key parameters analysis

In accordance with the out-of-plane buckling analysis, the strain energy of the in-plane buckling system can be shown in Eq. (51).

$$U_T^{in}=\frac{blE\kappa^2}{6}(t-z_{ns})^3+\frac{bl\nu_m G_m\kappa}{2}z_{ns}^2 +\frac{bl\nu_m G_m\lambda^2\kappa}{4\pi^2}\ln\left[\frac{4z_{ns}\sqrt{\nu_f}}{d\sqrt{\pi}}\right]+\frac{2bl\pi\nu_f E_f I_f\kappa}{\lambda^2 d^2}z_{ns}^2 \tag{51}$$

Fig. 5(a) shows the variation of strain energy of the in-plane buckling system with the relative neutral surface position. Similar to the out-of-plane buckling system, the in-plane buckling system likewise exhibits an energy minimum with the relative neutral surface position. As a result, the neutral surface and critical buckling positions are calculated using the minimum energy principle, which is compatible with the out-of-plane buckling system. The neutral surface and critical buckling positions are different for out-of-plane buckling and in-plane buckling owing to the distinct strain energy expressions, but the strain energy of the different components is barely impacted by the neutral surface position. Therefore, the expressions of neutral surface position and critical buckling position of the two systems can be considered the same.

Fig. 5(b) illustrates the variations of strain energy *Uin zz* and *Uin fb* with half-wavelength. The half-wavelength of the in-plane buckling system can be solved by using the minimum energy principle, as shown in Eq. (52). Similarly, the amplitude of fiber buckling can be obtained by the relationship between half-wavelength and amplitude.

$$\lambda^{in}=\left[\frac{8\pi^3\nu_f E_f I_f\left(z_{ns}^2-\frac{4C^2}{\kappa^2}\right)}{\nu_m G_m d^2\ln\left(\frac{z_{ns}\kappa}{2C}\right)}\right]^{\frac{1}{4}} \tag{52}$$

3.3. Stress analysis

The internal stresses of the matrix and fiber were analyzed to explore the damage mechanisms of SMPC experiencing in-plane buckling deformation. The tensile stress of fiber buckling in the buckling region is identical with Eq. (28), and the compressive/tensile stress in the X-direction of the non-buckling region is consistent with Eq. (29). The matrix stress can be divided into shear stress τ_{xy} and shear stress τ_{yz} in the buckling region, and the compressive/tensile stress σ_{xx} in the non-buckling region. The shear stress of the matrix in the X–Y plane can be given as:

$$\tau_{xy}=G_m\gamma_{xy}=-2G_m\sqrt{\kappa(z_{ns}-z)}\sin\left(\frac{\pi x}{\lambda}\right) \tag{53}$$

When $z=0$, $x=n\lambda/2$ ($n=0,1,2\cdots\cdots$), the shear stress reaches the maximum:

$$\tau_{xy,\max}=2G_m\sqrt{\kappa z_{ns}} \tag{54}$$

The shear stress τ_{yz} of the matrix in the Y-Z plane can be described as:

$$\tau_{yz}=G_m\gamma_{yz}=G_m\frac{\delta y}{\delta z}=\frac{G_m\kappa\lambda}{\pi\sqrt{\kappa(z_{ns}-z)}}\cos\left(\frac{\pi x}{\lambda}\right) \tag{55}$$

When $z=z_{cb}$, $x=n\lambda(n=0,1,2\cdots\cdots)$, shear stress τ_{yz} reaches maximum:

$$\tau_{yz,\max}=\frac{G_m\kappa\lambda}{\pi\sqrt{\kappa(z_{ns}-z_{cb})}} \tag{56}$$

Through the stress analysis of the matrix in the buckling region, the maximum stress appears at $z=0$ or $z=z_{cb}$. The stress analysis of the matrix at $z=0$ shows that when $x=n\lambda/2$, the maximum shear stress of the matrix can be expressed as shown in Eq. (57). The stress analysis of the matrix at $z=z_{cb}$ shows that when $x=n\lambda$, the shear stress $\tau_{z=z_{cb}}$ reaches the maximum (as shown in Eq. (58)).

$$\tau_{z=0}^{in},\max=2G_m\sqrt{\kappa z_{ns}} \tag{57}$$

$$\tau_{z=z_{cb},\max}^{in}=\frac{G_m\kappa\lambda}{\pi\sqrt{2C}} \tag{58}$$

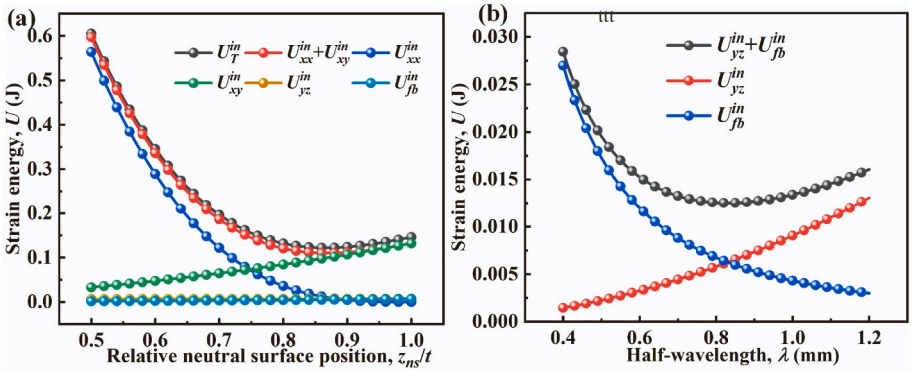

Fig. 5. (a) Partial strain energy variation with relative neutral surface position ($\lambda=0.89$ mm, $\kappa=0.05$ mm^{-1}); (b) Strain energy variation of *Uin zz* and *Uin fb* with half-wavelength ($z_{ns}=1.8$ mm, $\kappa=0.05$ mm^{-1}).

3.4. Critical damage curvature

The criterion of maximum shear stress and maximum tensile stress is adopted to judge whether SMPC is damaged in the in-plane buckling system, which is consistent with out-of-plane buckling analysis. The stress of matrix and fiber must be lower than their respective strengths, hence the internal stresses at the danger points need to satisfy Eq. (59). The critical damage curvature should be the minimum of the critical damage curvature corresponding to the internal stress of the matrix and fiber, as shown in Eq. (60).

$$\tau^{in}_{z=0,\max} \le \tau_s, \tau^{in}_{z=z_{cb},\max} \le \tau_s, \sigma^{in}_{fxx,\max} \le \sigma_{sf}, \sigma^{in}_{fb,\max} \le \sigma_{sf} \tag{59}$$

$$\kappa^{in}_{cf} = \min\left\{\kappa^{in}_{cf,z=0}, \kappa^{in}_{cf,z=z_{cb}}, \kappa^{in}_{cf,fxx}, \kappa^{in}_{cf,fxx}\right\} \tag{60}$$

4. Material and experimental methods

To verify the theoretical analysis of this study, unidirectional fiber reinforced SMPC was prepared and then a bending test was performed. The unidirectional fiber-reinforced SMPC was prepared by prepreg, with carbon fiber and shape memory epoxy resin serving as reinforcement and matrix, respectively (as shown in Table 1). The preparation scheme of SMPC is shown in Fig. 6(a). The laying angle of SMPC was 0°, and the number of layers was 8. After laying the prepreg, it was placed in an autoclave and vacuumed to 0.1 MPa. The curing procedures were 80 °C/3 h, 100 °C/3 h and 150 °C/5 h. The cured SMPC had a fiber volume content of about 30% and a dimension of 20 mm × 5 mm × 2 mm after cutting.

Out-of-plane buckling and in-plane buckling were generated by constraining displacement in the width and thickness directions, respectively (as shown in Fig. 6(b)). The displacement in the width direction of the SMPC was constrained by placing metal plates on both sides. The thickness direction displacement was constrained by placing a bendable thin metal plate inside the bend. Since the neutral surface position is very close to the outermost side of tension when critical damage occurs, it is assumed that the neutral surface position is located at the outermost side of tension.

5. Results and discussion

5.1. Strain energy analysis

Fig. 7 depicts the strain energy comparison between the out-of-plane and the in-plane buckling systems during bending. The results reveal that the strain energy of the out-of-plane buckling system is slightly higher than that of the in-plane buckling system, indicating that out-of-plane buckling requires more strain energy. Meanwhile, the total strain energy expressions of the two systems mainly distinguish in the two

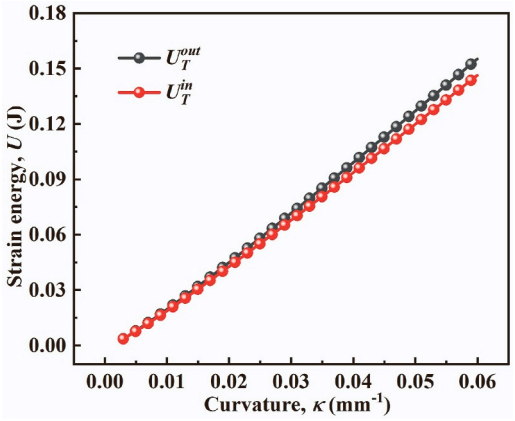

Fig. 7. Strain energy comparison between in-plane buckling system and out-of-plane buckling system during bending.

strain energies U_{fb} and U_{zz} (U_{yz}). The difference between the strain energy expressions (U_{zz} and U_y) of the two systems is that out-of-plane buckling is compressive/tensile strain energy, while in-plane buckling is shear strain energy. The expressions obtained by comparing the two strain energies are shown in Eqs. (61) and (62). It can be found that these two expressions are consistent. Since the matrix modulus E_m is greater than the shear modulus G_m of the matrix, the strain energy of out-of-plane buckling must be greater than that of in-plane buckling. Therefore, in-plane buckling is more likely to occur without external constraints during bending according to the minimum energy principle. However, out-of-plane buckling can be achieved by constraining the displacement of fiber buckling direction.

$$\frac{U^{out}_f}{U^{in}_f} = \left(\frac{\lambda^{in}}{\lambda^{out}}\right)^2 = \sqrt{\frac{E_m}{G_m}} \tag{61}$$

$$\frac{U^{out}_{zz}}{U^{in}_{yz}} = \frac{E_m}{G_m}\left(\frac{\lambda^{out}}{\lambda^{in}}\right)^2 = \sqrt{\frac{E_m}{G_m}} \tag{62}$$

5.2. Key parameters analysis

Fig. 8(a) and (b) compare the half-wavelength and amplitude of the out-of-plane and in-plane buckling systems during bending. The results demonstrate that the in-plane buckling system has a bigger half-wavelength and amplitude than the out-of-plane buckling system. By comparing the expressions of half-wavelength and amplitude of out-of-plane and in-plane buckling, the difference is that the shear modulus G_m of the matrix of in-plane buckling becomes the matrix modulus E_m of out-of-plane buckling. This is because the matrix in the Z-direction of the in-plane buckling system experiences shear deformation due to the

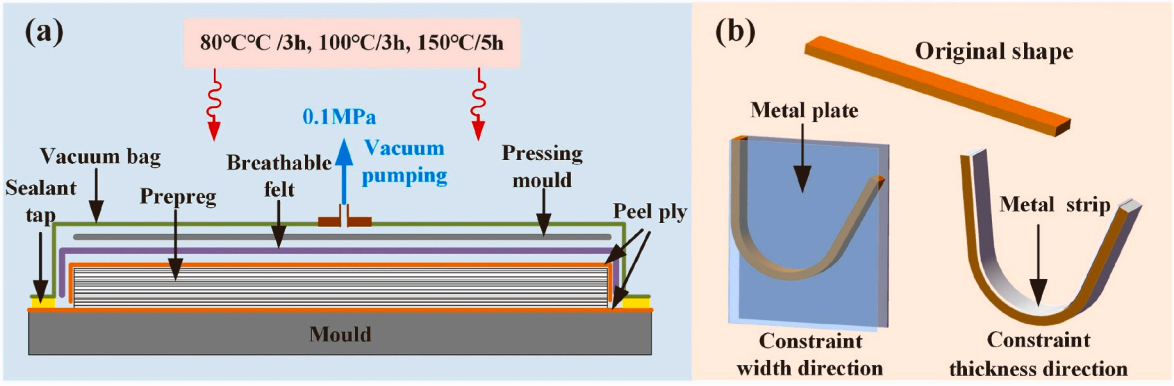

Fig. 6. (a) Manufacturing process diagram of SMPC; (b) Schematic diagram of SMPC bending test.

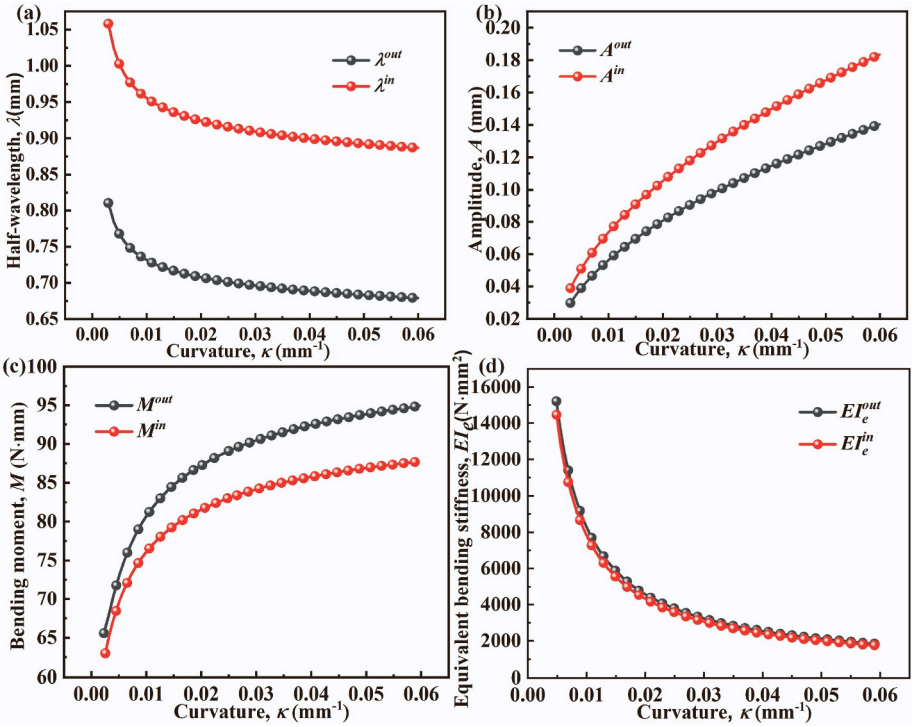

Fig. 8. Comparison of parameters of out-of-plane and in-plane buckling during bending: (a) half-wavelength; (b) amplitude; (c) bending moment; (d)equivalent bending stiffness.

inconsistent amplitude of adjacent fibers, while the matrix in the Z-direction of the out-of-plane buckling system has compressive/tensile deformation because of the inconsistent amplitude of adjacent fibers.

The bending moment comparison of out-of-plane and in-plane buckling during bending is shown in Fig. 8(c). The bending moment of out-of-plane buckling is higher than that of in-plane buckling, which is compatible with the strain energy, indicating that a big bending moment is required if out-of-plane buckling occurs. On the contrary, the out-of-plane buckling can provide a greater driving moment. Fig. 8 (b) shows the equivalent bending stiffness comparison of out-of-plane and in-plane buckling during bending. Out-of-plane buckling has a larger equivalent bending stiffness than in-plane buckling.

5.3. Damage mode analysis

Fig. 9 depicts the effects of thickness and fiber volume content on damage modes of out-of-plane and in-plane buckling. The findings demonstrate that the damage modes of in-plane buckling can be classified as delamination damage, matrix cracking damage and fiber tensile fracture damage. The out-of-plane buckling damage mode almost identical to the in-plane buckling damage mode. The difference is that when the fiber volume content is between 5–8.63% and the thickness is between 0.5–0.75 mm, the fiber buckling fracture damage may occur in the buckling region. When the fiber volume content of in-plane buckling is less than 9.28%, only tensile fracture damage occurs, which is independent of thickness. At the same time, in the same thickness and fiber volume content range, the area corresponding to the delamination

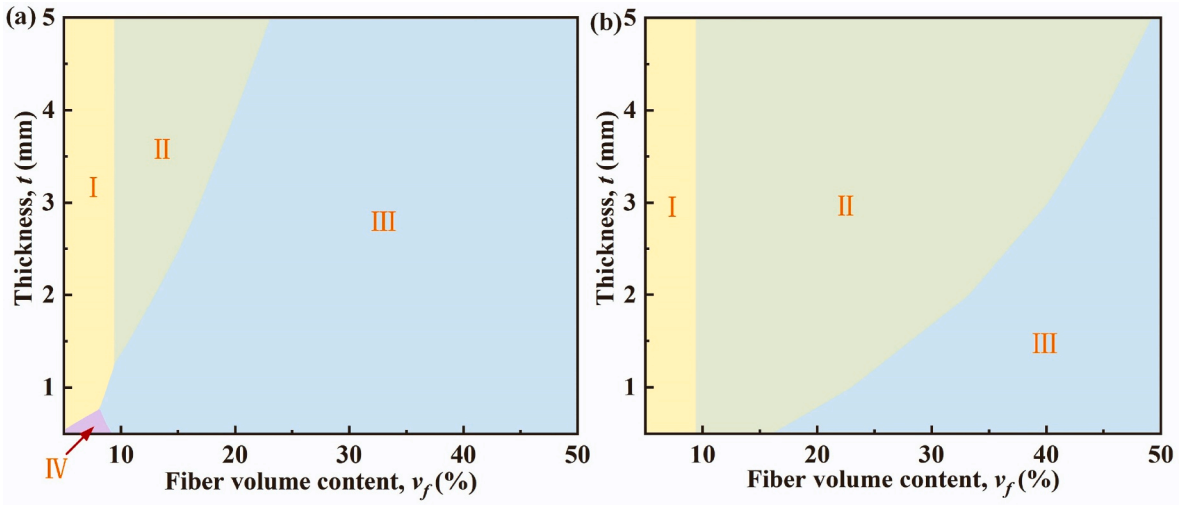

Fig. 9. Effects of thickness and fiber volume content on damage modes: (a) out-of-plane buckling; (b) in-plane buckling. I: fiber tensile fracture damage mode; II: matrix fracture damage mode; III: delamination damage mode; IV: Fiber buckling fracture damage mode.

damage of out-of-plane buckling is bigger than that of in-plane buckling, indicating that out-of-plane buckling is more vulnerable to delamination damage. Contrarily, in-plane buckling is more prone to matrix cracking damage. At the same thickness, with the increase of fiber volume content, the damage mode changes from fiber tensile fracture damage to matrix cracking damage, and then to delamination damage. It should be noted that the damage mode in Fig. 9 varies depending on the data in Tables 1 and 2

The shear stress of the matrix reaching the shear strength at $z = 0$ and $z = z_{cb}$ corresponds to the matrix cracking damage and delamination damage, respectively. When the shear stress ratio at $z = 0$ and $z = z_{cb}$ is less than 1, delamination damage is more probable at $z = z_{cb}$. When the ratio is greater than 1, the matrix cracking is more likely to occur at $z = 0$. Fig. 10(a) and (b) show the variation of shear stress ratios at $z = 0$ and $z = z_{cb}$ with matrix modulus and curvature for out-of-plane and in-plane buckling, respectively. The findings reveal that with the increase of bending curvature, the shear stress ratio at $z = 0$ and $z = z_{cb}$ gradually rises. This indicates that the greater the bending curvature is, the greater the risk of delamination damage is. The shear stress ratio of out-of-plane buckling at $z = 0$ and $z = z_{cb}$ is less than that of in-plane buckling under the same matrix modulus, which signifies that in-plane buckling is more vulnerable to matrix cracking damage than out-of-plane buckling.

Fig. 10(c) and (d) show the variation of shear stress ratios at $z = 0$ and $z = z_{cb}$ with fiber modulus and curvature for out-of-plane and in-plane buckling, respectively. The results show that the variation trends of out-of-plane and in-plane buckling are basically the same. With the increase of bending curvature and fiber modulus, the shear stress ratio at $z = 0$ and $z = z_{cb}$ progressively decreases. This demonstrates that the bigger the curvature and fiber modulus are, the more prone to delamination damage is. The shear stress ratio of out-of-plane buckling at $z = 0$ and $z = z_{cb}$ is less than that of in-plane buckling under the same fiber modulus, which signifies that out-of-plane buckling is more vulnerable to delamination damage than in-plane buckling.

5.4. Critical damage analysis

Fig. 11(a) and (b) show the variations of critical buckling curvature with thickness at different fiber volume content for out-of-plane and in-plane buckling, respectively. The parameters of carbon fiber in Table 3 are used in the figure. The results reveal that with the increase of material thickness, the critical damage curvature reduces in varying degrees, implying that the greater the thickness is, the more probable damage will occur during bending. When the fiber volume content is greater than 5%, the critical damage curvature decreases gradually with the rise of fiber volume content, indicating that material damage is more likely to occur. When the fiber volume content is 5%, owing to the change of damage mode, the critical damage curvature is less than the critical damage curvature with 20% fiber volume content. Simultaneously, the critical damage curvature of in-plane buckling is less than that of out-of-plane buckling, indicating that out-of-plane buckling is more vulnerable to damage.

Fig. 11(c) and (d) shows the variations of critical buckling curvature with matrix modulus at different fiber moduli for out-of-plane and in-plane buckling, respectively. The critical damage curvature of fibers with various moduli drops to varying degrees as the matrix modulus increases, suggesting that the higher the matrix modulus is, the more probable damage will occur. The curve has a turning point caused by switching the damage mode from delamination to matrix cracking. At the same time, with the increase of fiber modulus, the critical damage curvature also reduces, making the selection of high modulus carbon fiber more vulnerable to damage. It is worth noting that SMPC-based structures can be designed through the critical damage curvature obtained in this study.

5.5. Experimental verification

Fig. 12 compares the theoretical prediction and experimental results of critical damage curvature for out-of-plane buckling and in-plane buckling, respectively. The theoretical results are in order of magnitude compatible with the experimental results, and they are in good agreement. At the same time, the damage mode in the experiment also corresponds well to the figure, which can also be confirmed by the change trend of critical damage. Table 4 compares theoretical and experimental results for half-wavelength and amplitude of fiber

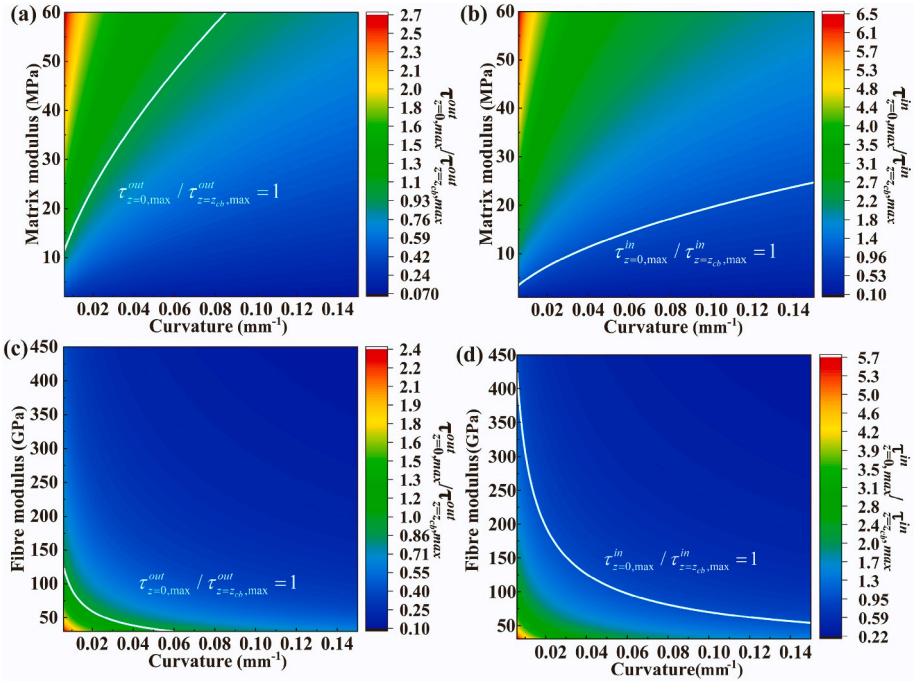

Fig. 10. (a) and (b) are the variation of shear stress ratios at $z = 0$ and $z = z_{cb}$ with matrix modulus and curvature for out-of-plane and in-plane buckling, respectively; (c) and (d) are the variation of shear stress ratios at $z = 0$ and $z = z_{cb}$ with fiber modulus and curvature for out-of-plane and in-plane buckling, respectively.

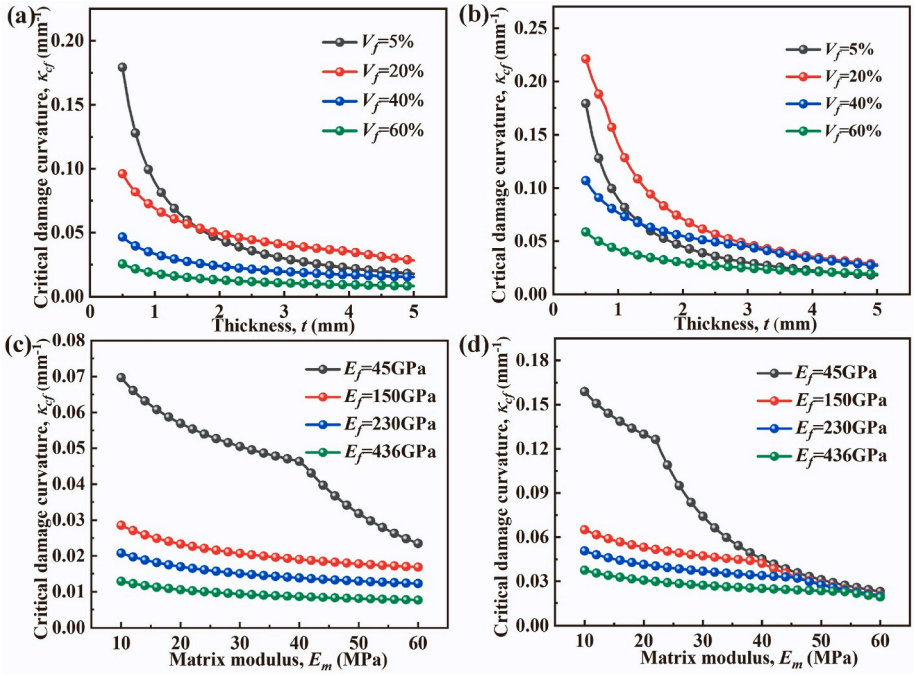

Fig. 11. (a) and (b) are the variations of critical buckling curvature with thickness at different fiber volume content for out-of-plane and in-plane buckling, respectively; (c) and (d) are the variations of critical buckling curvature with matrix modulus at different fiber moduli for out-of-plane and in-plane buckling, respectively.

Table 3
Carbon fiber parameters.

Carbon fiber	Parameter			
	Diameter (μm)	Tensile modulus (GPa)	Tensile strength (MPa)	Elongation at break (%)
# 1	8	45	1100	2.4
# 2	8	150	3000	2
# 3	7	230	3530	1.5
# 4	5	436	4210	1

buckling during bending. The theoretical value was calculated using the theoretical half-wavelength and maximum amplitude, and the experimental value was calculated using the experimentally measured half-wavelength and the maximum amplitude. In order of magnitude, the theoretical prediction value and the experimental value of SMPC in the bending process are completely consistent, and the specific results are also basically consistent.

According to the critical damage data, SMPC can achieve a large folding ratio through the micro buckling of local fibers. Notably, the SMPC-based lenticular tube was designed and optimized based on the utilization of this study, and the on-orbit deployment of the flexible solar array system was successfully demonstrated, which can serve for ultra-large flexible solar array systems based on SMPCs in the future (as shown in Fig. 13) (Lan et al., 2020).

6. Conclusions

In this study, the buckling behavior and damage mechanism of out-of-plane and in-plane buckling of unidirectional fiber-reinforced SMPC were investigated. The theoretical analysis findings have an important theoretical significance for structural design based on SMPC. Several conclusions are summarized as follows:

a) The expressions of strain energy and key parameters for out-of-plane and in-plane buckling systems are developed. Out-of-plane buckling has higher strain energy and bending moment, and smaller half-wavelength and amplitude than in-plane buckling. SMPC is more prone to in-plane buckling when bending without constraints.

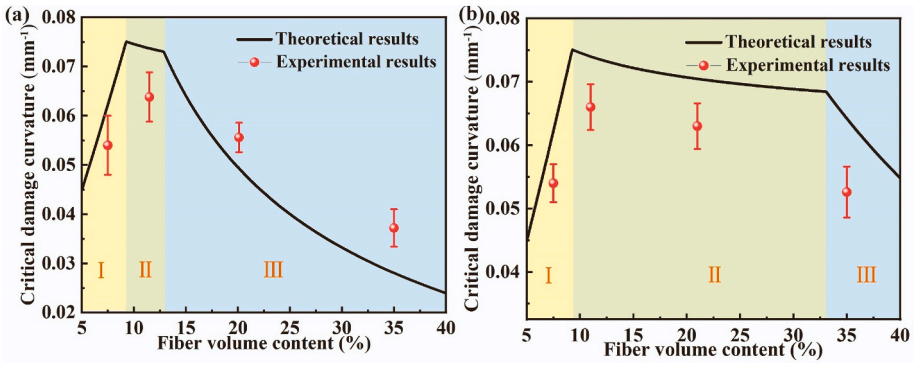

Fig. 12. Comparison between theoretical prediction and experimental results of critical damage curvature: (a) out of plane buckling; (b) in-plane buckling. I: fiber tensile fracture damage mode; II: matrix fracture damage mode; III: delamination damage mode.

Table 4
Comparison of theoretical and experimental results of half-wavelength and maximum amplitude of fiber buckling.

Buckling status	Curvature (mm^{-1})	Half-wavelength (mm)		Maximum amplitude (mm)	
	Design value	Theoretical value	Experimental value	Theoretical value	Experimental value
Out-of-plane buckling	0.02	0.707	0.62 ± 0.02	0.08	0.06 ± 0.06
	0.03	0.696	0.60 ± 0.06	0.099	0.08 ± 0.10
	0.04	0.689	0.65 ± 0.10	0.115	0.10 ± 0.08
In-plane buckling	0.02	0.924	0.82 ± 0.04	0.105	0.09 ± 0.02
	0.03	0.909	0.78 ± 0.08	0.129	0.12 ± 0.01
	0.04	0.899	0.76 ± 0.12	0.150	0.16 ± 0.06

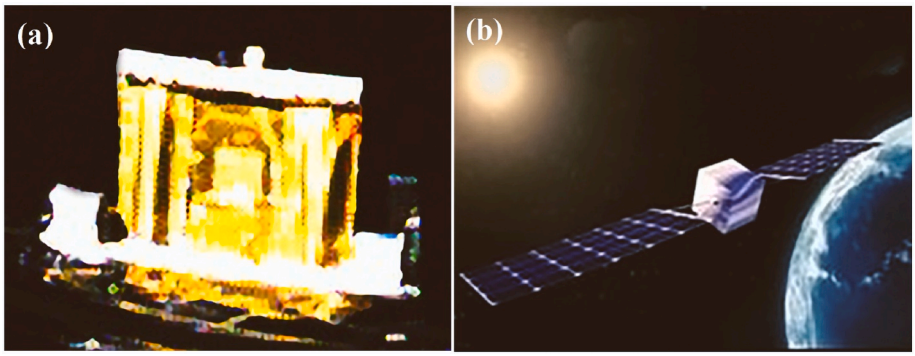

Fig. 13. Flexible solar array system based on SMPC lenticular tube: (a) on orbit demonstration: (b) super-large flexible solar array system based on SMPCs.

b) Based on the material parameters in this study, the damage modes of in-plane buckling can be classified as delamination damage, matrix cracking damage and fiber tensile fracture damage. Out-of-plane buckling has one more fiber buckling fracture damage mode than in-plane buckling. The damage mode changes from the fiber tensile fracture damage to the matrix cracking damage, and then to the delamination damage as the fiber volume content increases. When the fiber volume content is less than a certain value, only fiber tensile fracture damage mode will occur, which is independent of the thickness.
c) Out-of-plane buckling is more prone to damage than in-plane buckling, and out-of-plane buckling is more vulnerable to delamination damage. On the contrary, in-plane buckling is more prone to matrix cracking damage. Reducing the fiber modulus can reduce the occurrence of delamination damage. The greater the SMPC thickness is, the more easily damage occurs. Finally, the theoretical analysis of the damage limit is verified by experiments.

Author statement

I have made substantial contributions to the conception or design of the work; or the acquisition, analysis, or interpretation of data for the work. I have drafted the work or revised it critically for important intellectual content. I agree to be accountable for all aspects of the work in ensuring that questions related to the accuracy or integrity of any part of the work are appropriately investigated and resolved.

I would like to declare on behalf of my co-authors that the work described was original research that has not been published previously, and not under consideration for publication elsewhere, in whole or in part. All the authors listed have approved the manuscript. We deeply appreciate your consideration of our manuscript, and we look forward to receiving comments from the reviewers. If you have any queries, please don't hesitate to contact me at the address below.

Declaration of competing interest

The authors declare that they have no known competing financial interests or personal relationships that could have appeared to influence the work reported in this paper.

Data availability

Data will be made available on request.

Acknowledgements

The authors would like to thank the Heilongjiang Touyan Innovation Team Program. This work is supported by the National Natural Science Foundation of China (Grant No. 11632005, 11872020).

References

Boudjellal, A., Trache, D., Khimeche, K., Hafsaoui, S.L., Bougamra, A., Tcharkhtchi, A., Durastanti, J.-F., 2020. Stimulation and reinforcement of shape-memory polymers and their composites: a review. J. Thermoplast. Compos. Mater. 9, 1–34.
Das, B., Prasad, K.E., Ramamurty, U., Rao, C., 2009. Nano-indentation studies on polymer matrix composites reinforced by few-layer graphene. Nanotechnology 20, 125705.
Dong, Y., Ni, Q.-Q., Li, L., Fu, Y., 2014. Novel vapor-grown carbon nanofiber/epoxy shape memory nanocomposites prepared via latex technology. Mater. Lett. 132, 206–209.
Dong, Y., Ni, Q.Q., 2015. Effect of vapor-grown carbon nanofibers and in situ hydrolyzed silica on the mechanical and shape memory properties of water-borne epoxy composites. Polym. Compos. 36, 1712–1720.
Francis, W., Lake, M., Schultz, M., Campbell, D., Dunn, M., Qi, H.J., 2007. Elastic memory composite microbuckling mechanics: closed-form model with empirical correlation. In: 48th AIAA/ASME/ASCE/AHS/ASC Structures, Structural Dynamics, and Materials Conference.
Gall, K., Mikulas, M., Munshi, N.A., Beavers, F., Tupper, M., 2016. Carbon fiber reinforced shape memory polymer composites. J. Intell. Mater. Syst. Struct. 11, 877–886.
Gall, K., Mikulas, M., Munshi, N.A., Beavers, F., Tupper, M.J., 2000. Carbon fiber reinforced shape memory polymer composites. J. Intell. Mater. Syst. Struct. 11, 877–886.
Garces, I.T., Ayranci, C., 2021. Advances in additive manufacturing of shape memory polymer composites. Rapid Prototyp. J. 27, 379–398.
Glock, S., Canal, L.P., Grize, C.M., Michaud, V.J., Technology, 2015. Magneto-mechanical actuation of ferromagnetic shape memory alloy/epoxy composites. Compos. Sci. Technol. 114, 110–118.
Gu, L., Jiang, Y., Hu, J., 2019. Structure design and property of spider silk-inspired shape memory materials. Mater. Today 16, 1491–1496.
Guo, J., Liu, J., Wang, Z., He, X., Hu, L., Tong, L., Tang, X., 2017. A thermodynamics viscoelastic constitutive model for shape memory polymers. J. Alloys Compd. 705, 146–155.

Lan, X., Hao, S., Liu, L., Liu, Y., Leng, J., 2019. Macroscale bending large-deformation and microbuckling behavior of a unidirectional fiber-reinforced soft composite. J. Compos. Mater. 54, 243–257.
Lan, X., Liu, L., Liu, Y., Leng, J., Du, S., 2014. Post microbuckling mechanics of fibre-reinforced shape-memory polymers undergoing flexure deformation. Mech. Mater. 72, 46–60.
Lan, X., Liu, L., Zhang, F., Liu, Z., Wang, L., Li, Q., Peng, F., Hao, S., Dai, W., Wan, X., Tang, Y., Wang, M., Hao, Y., Yang, Y., Yang, C., Liu, Y., Leng, J., 2020. World's first spaceflight on-orbit demonstration of a flexible solar array system based on shape memory polymer composites. Sci. China Technol. Sci. 63, 1436–1451.
Leng, J., Lv, H., Liu, Y., Du, S., 2007. Electroactivate shape-memory polymer filled with nanocarbon particles and short carbon fibers. Appl. Phys. Lett. 91, 144105.
Leng, J., Lv, H., Liu, Y., Du, S., 2008. Synergic effect of carbon black and short carbon fiber on shape memory polymer actuation by electricity. J. Appl. Phys. 104, 104917.
Leng, J., Wu, X., Liu, Y., 2009. Effect of a linear monomer on the thermomechanical properties of epoxy shape-memory polymer. Compos. B Eng. 18, 095031.
Li, F., Leng, J., Liu, Y., Remillat, C., Scarpa, F., 2020. Temperature dependence of elastic constants in unidirectional carbon fiber reinforced shape memory polymer composites. Mech. Mater. 148.
Liu, R., Kuang, X., Deng, J., Wang, Y.C., Wang, A.C., Ding, W., Lai, Y.C., Chen, J., Wang, P., Lin, Z., 2018. Shape memory polymers for body motion energy harvesting and self-powered mechanosensing. Adv. Mater. 30, 1705195.
Liu, Y., Du, H., Liu, L., Leng, J., 2014. Shape memory polymers and their composites in aerospace applications: a review. Smart Mater. Struct. 23, 023001.
Liu, Z., Lan, X., Bian, W., Liu, L., Li, Q., Liu, Y., Leng, J., 2020. Design, material properties and performances of a smart hinge based on shape memory polymer composites. Compos. B Eng. 193, 108056.
Lu, H., Lei, M., Zhao, C., Yao, Y., Gou, J., Hui, D., Fu, Y., 2015. Controlling Au electrode patterns for simultaneously monitoring electrical actuation and shape recovery in shape memory polymer. Compos. B Eng. 80, 37–42.
Luo, L., Zhang, F., Leng, J., 2021. Multi-performance shape memory epoxy resins and their composites with narrow transition temperature range. Compos. Sci. Technol. 213, 108899.
Luo, L., Zhang, F., Leng, J., 2022. Shape memory epoxy resin and its composites: from materials to applications. Research 2022, 9767830.
Melly, S.K., Liu, L., Liu, Y., Leng, J., 2020. Active composites based on shape memory polymers: overview, fabrication methods, applications, and future prospects. J. Mater. Sci. 55, 10975–11051.
Melly, S.K., Liu, L., Liu, Y., Leng, J., 2021. A review on material models for isotropic hyperelasticity. Int J Mech Sys Dyna 1, 71–88.
Patel, K.K., Purohit, R., 2018. Future prospects of shape memory polymer nano-composite and epoxy based shape memory polymer-a review. Mater. Today 5, 20193–20200.
Shaffer, M.S., Windle, A., 1999. Fabrication and characterization of carbon nanotube/poly (vinyl alcohol) composites. Adv. Mater. 11, 937–941.
Shin, Y.C., Lee, J.B., Kim, D.H., Kim, T., Alexander, G., Shin, Y.M., Park, J.Y., Baek, S., Yoon, J.K., Lee, Y.J., 2019. Development of a shape-memory tube to prevent vascular stenosis. Adv. Mater. 31, 1904476.
Shojaei, A., Sharafi, S., Li, G., 2015. A multiscale theory of self-crack-healing with solid healing agent assisted by shape memory effect. Mech. Mater. 81, 25–40.
Thostenson, E.T., Chou, T.-W., 2002. Aligned multi-walled carbon nanotube-reinforced composites: processing and mechanical characterization. Adv. Mater. 35, L77.
Wang, W., Liu, D., Liu, Y., Leng, J., Bhattacharyya, D.J., Technology, 2015. Electrical actuation properties of reduced graphene oxide paper/epoxy-based shape memory composites. Mech. Mater. 106, 20–24.
Wei, Z., Sandstroröm, R., Miyazaki, S., 1998. Shape-memory materials and hybrid composites for smart systems: Part I Shape-memory materials. J. Mater. Sci. 33, 3743–3762.
Xia, Y., He, Y., Zhang, F., Liu, Y., Leng, J., 2021. A review of shape memory polymers and composites: mechanisms, materials, and applications. Adv. Mater. 33, e2000713.
Xie, T., 2011. Recent advances in polymer shape memory. Polymer 52, 4985–5000.
Xin, X., Liu, L., Liu, Y., Leng, J., 2019. Mechanical models, structures, and applications of shape-memory polymers and their composites. Acta Mech. Solida Sin. 32, 535–565.
Xiong, Z., Jin, D., Yang, Y., Zeng, D., 2014. A theoretical investigation into the orientation of buckling direction of the reinforcing fibers in EMC laminate. J. Wuhan Univ. Technol.-Materials Sci. Ed. 29, 148–153.
Xiong, Z.Y., Wang, Z.D., Li, Z.F., Chang, R.N., 2008. Micromechanism of deformation in EMC laminates. Mater. Sci. Eng. 496, 323–328.
Yoonessi, M., Shi, Y., Scheiman, D.A., Lebron-Colon, M., Tigelaar, D.M., Weiss, R., Meador, M.A., 2012. Graphene polyimide nanocomposites; thermal, mechanical, and high-temperature shape memory effects. ACS Nano 6, 7644–7655.
Zhang, J., Dui, G., Liang, X., 2018. Revisiting the micro-buckling of carbon fibers in elastic memory composite plates under pure bending. Int. J. Mech. Sci. 136, 339–348.
Zhang, Y.F., Zhang, N., Hingorani, H., Ding, N., Wang, D., Yuan, C., Zhang, B., Gu, G., Ge, Q., 2019. Fast-response, stiffness-tunable soft actuator by hybrid multimaterial 3D printing. Adv. Funct. Mater. 29, 1806698.